Vicarious Calibration of the Long Near Infrared Band: Cross-Sensor Differences in Sensitivity

Brian B. Barnes[A*], Sean W. Bailey[B], Chuanmin Hu[A], Bryan A. Franz[B]

Abstract— **Numerous assumptions and approximations are employed when translating satellite-derived radiance to surface remote sensing reflectance (R_{RS}) for ocean color applications. Among these is the vicarious calibration coefficient (g) of the 'long' near infrared band (NIR_L) used for atmospheric correction. For this band, the pre-launch calibration has always been deemed sufficient [thus $g(NIR_L)$ = 1.00] as long as other bands are vicariously calibrated. Recent research, however, suggests that MODIS/Aqua R_{RS} time series are quite sensitive to $g(NIR_L)$ (and associated vicarious gains in other bands). In this work, we assessed the sensitivity of VIIRS/SNPP R_{RS} to NIR_L calibration, and compared our results to previous MODIS/Aqua and SeaWiFS/OrbView2 analysis. In doing so, we note $g(NIR_L)$ sensitivities of mission-averaged R_{RS} timeseries are lower for VIIRS and SeaWiFS, relative to MODIS. At the scale of monthly climatologies, however, all sensors show prominent $g(NIR_L)$ sensitivity, with that of SeaWiFS being the most substantial. These findings informed simulation analyses, whereby we identified signal-to-noise ratio (SNR) and radiant path geometry, as well as their interaction, as having notable impacts on $g(NIR_L)$ sensitivity. As such, $g(NIR_L)$ sensitivity is a necessary consideration for reflectance uncertainty budgets, especially for sensors with higher NIR SNR or particular prevailing radiant path geometries. Given the geometry components embedded within $g(NIR_L)$ sensitivity, such studies should be coupled with cross-sensor intercalibrations (e.g., using simultaneous same view measurements) toward minimizing NIR_L errors between satellite instruments, but such efforts will not completely remediate remaining cross-sensor biases in R_{RS}.**

Index Terms— **System vicarious calibration, ocean color, MODIS/Aqua, SeaWiFS, VIIRS/SNPP, ocean gyres**

I. INTRODUCTION

AS the duration of the satellite ocean color dataset lengthens and as new satellite-borne instruments are brought into mainstream use, the necessity of mechanisms to intercalibrate sensors towards consistent, unbiased merged-sensor datasets becomes salient. Indeed, numerous previous works have suggested methods by which to correct merged-sensor datasets [1], [2], while offering a suite of explanations as to the primary cause(s) for any cross-sensor disagreements or discontinuities [3]–[5]. Among these potential causes is the calibration of the 'long' near infrared band (NIR_L), which is used within atmospheric correction of the satellite-measured total radiance (L_t). For a variety of practical reasons, this band has never been vicariously calibrated for operational satellite ocean color data processing [6]. Instead, the pre-launch characterization of this band is considered to be sufficient, as [6] showed $\pm 5\%$ changes in the calibration of this NIR_L band, after subsequent calibration of all other bands, have acceptable impact on downstream remote sensing reflectance (R_{RS}) retrievals in the visible wavelengths. Here, R_{RS} (in sr^{-1}) is defined as the ratio of water leaving radiance (L_w, in mW cm^{-2} μm^{-1} sr^{-1}) to downwelling irradiance (E_d, in mW cm^{-2} μm^{-1}). Stemming from [6], the system vicarious calibration (SVC) coefficient (often termed 'gain' or 'g-factor,' denoted g) for the NIR_L band is set at 1.00. Subsequent to this assumption, SVC is performed for all other bands to establish band-specific gains [7]. Note that SVC scales satellite measured top-of-atmosphere radiance (L_t) to *in situ* L_w, propagated through the atmosphere using the atmospheric correction algorithms (to approximate L_t). SVC thereby corrects biases in the combined sensor - atmospheric correction system. SVC is one component of the broader calibration of an instrument, which includes pre-launch and on-orbit efforts to correct band-specific changes in sensor responsiveness resulting from temporal degradation, temperature, scan angle, and other instrument-specific effects.

The assumption of visible R_{RS} insensitivity (within target uncertainty of 5%) to $\pm 5\%$ errors in g(NIR_L) was largely informed by simulations [6]. Recent research, however, suggests satellite-collected ocean color data show substantial sensitivity to the NIR_L calibration [8]. Specifically, [8] noted roughly 2-4% changes in overall mean MODIS/A [Moderate Resolution Imaging Spectroradiometer onboard Aqua] R_{RS}(547) in ocean gyres resulting from $\pm 5\%$ changes in g(NIR_L), with much larger sensitivities observed at finer timescales. Notably, this sensitivity varied according to hemispheric season, with higher sensitivity in winter and lower sensitivity in summer. Additionally, looking at MODIS/A and VIIRS/SNPP [Visible Infrared Imaging Radiometer Suite onboard the Suomi National Polar-orbiting Partnership satellite] data, [9]–[11] identified a 3 – 3.5% difference in NIR_L as measured between the two sensors. Calibrating VIIRS NIR_L

to match MODIS NIR$_L$ (and subsequently revising VIIRS SVC) resulted in partial improvement in cross-sensor continuity of downstream geophysical products [11].

In this paper, we combine new analysis of VIIRS/SNPP NIR$_L$ calibration sensitivity with previous such assessments for MODIS/A and SeaWiFS [Sea-viewing Wide Field-of-View Sensor onboard OrbView2]. In doing so, our objectives were to (1) quantify sensitivity of VIIRS remote sensing reflectance (R_{RS}), particularly at 551 nm, to changes in $g(862)$ (for VIIRS, the NIR$_L$ band is centered at 862 nm), and thereby (2) identify $g(862)$ for which the resultant $R_{RS}(551)$ time series is the most internally consistent. From these results, we also (3) compared $g(\text{NIR}_L)$ sensitivity between sensors and assessed potential causes for cross-sensor similarities and differences, and subsequently (4) recommend general approaches for establishment of $g(\text{NIR}_L)$ across ocean color sensors.

II. METHODS

This work combines new VIIRS $g(\text{NIR}_L)$ sensitivity analyses with previously completed assessments of MODIS/A and SeaWiFS, both of which are detailed in [8]. The overarching premise of all of these analyses was to quantify impacts of the $g(\text{NIR}_L) = 1.00$ assumption on downstream geophysical products (especially R_{RS} in the green wavelengths). To do so, these works all followed a similar general process: (1) establish a discrete $g(\text{NIR}_L) \neq 1.00$; (2) using this $g(\text{NIR}_L)$, calculate $g(\text{NIR}_S)$ ('short' near infrared band) using data from the South Pacific Gyre [7]; (3) using $g(\text{NIR}_L$ and $\text{NIR}_S)$, determine $g(\text{VIS})$ (visible bands) using marine optical buoy (MOBY) data [7]; and (4) reprocess the entire sensor dataset to derive $R_{RS}(\text{green})$ using this new gain suite and the same standard processing as with the original gain suite. These steps (1-4) were then repeated for a number of different $g(\text{NIR}_L)$, with the resultant $R_{RS}(\text{green})$ time series compared to the original dataset [$g(\text{NIR}_L) = 1.00$] as well as between each other. Note that for simplicity, throughout this paper, "changes in $g(\text{NIR}_L)$" actually refers to "changes in the gain suite corresponding to the changes in $g(\text{NIR}_L)$."

A. Previous studies (SeaWiFS and MODIS)

For the SeaWiFS analysis, the entire global radiance dataset was reprocessed with three different gain suites. For MODIS, 1.4E6 gain suites were tested, but only at 25 discrete locations within ocean gyres. Within the current study, results from only ten MODIS gain suites (of 1.4E6 tested in [8]) were considered, corresponding to those calculated using the exact steps (1-4) listed above (see Table III in [8]).

B. New processing (VIIRS)

For VIIRS analyses, we considered nine initial $g(862)$ values, evenly spaced from 0.95 – 1.05. Using the approach of [7], SVC was performed using each of these $g(\text{NIR}_L)$ as the 'pre-launch' characterization, thereby defining the nine gain suites shown in Table I. As this process exactly matches currently operational procedures, the derived gain suite for $g(862) = 1.00$ exactly matched extant SVC coefficients. Data quantity (N) and standard deviation (σ) for these SVCs varied slightly owing to

TABLE I
VIIRS SVC COEFFICIENTS, DERIVED USING NINE INITIAL $g(862)$, INCLUDING N AND σ RANGES FROM AMONG THOSE NINE SVC [7].

	$g(410)$	$g(443)$	$g(486)$	$g(551)$	$g(671)$	$g(775)$	$g(862)$
	0.9715	0.9504	0.9789	0.9689	0.9651	0.9565	0.9500
	0.9724	0.9517	0.9809	0.9724	0.9718	0.9654	0.9625
	0.9735	0.9532	0.9829	0.9756	0.9780	0.9742	0.9750
	0.9747	0.9547	0.9851	0.9791	0.9846	0.9831	0.9875
	0.9763	0.9565	0.9876	0.9827	0.9914	0.9918	1.0000[*]
	0.9778	0.9584	0.9900	0.9861	0.9979	1.0004	1.0125
	0.9790	0.9599	0.9921	0.9893	1.0040	1.0090	1.0250
	0.9801	0.9613	0.9940	0.9924	1.0101	1.0174	1.0375
	0.9806	0.9621	0.9954	0.9952	1.0161	1.0260	1.0500
σ	0.0124	0.0119	0.0125	0.0094	0.0062	0.0147	-
range[†]	0.0127	0.0121	0.0126	0.0097	0.0066	0.0155	-
N	207	207	207	207	207	736	-
range[†]	215	215	215	215	215	793	-

[*]Current default gain configuration.
[†]SVC for each initial $g(862)$ included a specific N points, and a unique σ about each derived $g(\text{VIS or NIR}_S)$. As these values did not vary greatly among the various SVCs, only the ranges are reported here.

TABLE II
STUDY AREAS

Gyre (Abbreviation)	Geographic Range (°N, °E)				VIIRS Data Quantity
	N	S	E	W	
N Atlantic (N Atl)	27	22	-45	-70	1.26E8
S Atlantic (S Atl)	-12.5	-22.5	-25	-32	7.54E7
N Pacific (N Pac)	20	10	165	150	8.25E7
S Pacific (S Pac)	-20	-30	-100	-125	1.80E8
S Indian (S Ind)	-21	-30	90	70	8.24E7

larger numbers of satellite data being flagged as questionable (i.e., clouds) with increasing $g(862)$ (Table I).

All VIIRS/SNPP Level-1A (L1A) data (02 January 2012 – 11 September 2020) with coverage within any of five ocean gyres (Table II) were accessed from the NASA archives. These L1A files were processed to Level-2 (L2) nine times, each using a separate gain set (Table I), thereby resulting in nine distinct time series of $R_{RS}(551)$ in each of the five ocean gyres. Overall gyre-specific mean ($\bar{x}$) and σ were determined for each gyre, as were monthly climatologies (MC), spanning all years of the satellite mission. Data identified as suspect by any of the L2 processing flags used for masking data in Level-3 (L3) global composites were removed from further analysis [12], as were pixels with sensor zenith > 40°. For fair comparison, any pixel excluded from any one (of the nine) $g(862)$ dataset was also excluded from all other datasets.

Daily mean (x_t) and 31-day moving mean (y_t) time series of $R_{RS}(551)$ were also calculated, with the deviation between these two determined in reflectance units (sr^{-1}; as Mean Absolute Deviation; MAD) and percent units (Mean Absolute Percent Deviation; MAPD). Specifically,

$$MAD = \frac{1}{N} \sum_{t=0}^{N} |x_t - y_t|,$$

$$MAPD = \frac{100}{N} \sum_{t=1}^{N} (|x_t - y_t|)/y_t,$$

where t corresponds to the date within the time series and center date of the moving mean ($N = 3,176$; 02 Jan 2012 – 11 Sept 2020). MAD and MAPD thus quantify the temporal stability of the $R_{RS}(551)$ time series (i.e., how closely daily-scale data track

their monthly moving mean). For each dataset, Pearson's correlation coefficient (r) was determined for lag-1 day autocorrelation (i.e., how variable are day-to-day x_t).

Pursuant to objective 2, these MAD, MAPD, and r metrics were all calculated to identify the $g(862)$ which produced the most 'realistic' $R_{RS}(551)$. The necessity for this approach lies in the realities that (1) gyre-scale $R_{RS}(551)$ time series are impossible to construct other than from satellite platforms, but (2) satellite datasets themselves are sensitive to $g(\mathrm{NIR_L})$. As such, the terms MAD, MAPD, and r were operationalized to quantify adherence to a logical argument that $R_{RS}(551)$ should change gradually in ocean gyres. The gain suites that produced high r and/or low MAD and MAPD would thus be considered more temporally coherent and therefore more realistic.

All metrics were separately recalculated to ensure fair comparison between the VIIRS analyses and previous MODIS results [8], whereby the VIIRS dataset was subset to match the exact conditions used in the former analyses. Specifically, we restricted the VIIRS dataset to pixels targeting only 25 discrete locations per gyre and duplicated the more strict data exclusion techniques specified in [8] (i.e., data were excluded if indicated by any of the Level-2 processing flags).

Where expedient in the following sections, the first letter of a sensor is used in referring to individual wavebands (e.g., S865, M869, and V862 are $\mathrm{NIR_L}$ bands). Although none of the analyses included a 'band shift,' for the clear ocean waters considered here, $R_{RS}(555) \approx 0.91 R_{RS}(547) \approx 0.94 R_{RS}(551)$ [13].

C. Geometry and SNR

Towards objective 3, we also investigated potential underlying causes for $g(\mathrm{NIR_L})$ sensitivity. As $g(\mathrm{NIR_L})$ sensitivity is inherently a processing artifact [R_{RS} for a target does not change just because $g(\mathrm{NIR_L})$ changes], and NASA ocean color processing (including SVC and atmospheric correction) are standardized across the various sensors, any cross-sensor differences in $g(\mathrm{NIR_L})$ sensitivity must be traceable to sensor- or platform-specific characteristics. Of note, satellite orbit differs between SeaWiFS, MODIS, and VIIRS, and radiant path geometry (which is a function of the orbit) is an explicit factor in calculation of multiple atmospheric component radiances. Additionally, SNRs of these three sensors are quite different, impacting the precision of retrieved R_{RS} datasets, which may potentially elucidate (or obscure) $g(\mathrm{NIR_L})$ sensitivity.

To directly assess any such potential radiant path and SNR impacts, we performed simulation analyses through which we processed $L_{typical}$ spectra (as reported in [14]) to derive $R_{RS}(547)$ at various SNR, solar zenith (θ_S), sensor zenith (θ_V), and relative azimuth ($\Delta\Phi$) angle configurations. Linear interpolation was used to calculate $L_{typical}$ at θ_S not directly listed in [14]. To simulate various SNR, spectrally incoherent noise was added to $L_{typical}$ values in the $\mathrm{NIR_L}$ and $\mathrm{NIR_S}$ bands. This was effectuated (using $\mathrm{NIR_L}$ as an example) by randomly selecting from a Gaussian distribution with mean of $L_{typical}(\mathrm{NIR_L})$ and standard deviation of $L_{typical}(\mathrm{NIR_L})/\mathrm{SNR}$. For each geometry configuration and SNR tested (100, 250, 500, 750, 1000, and ∞), 1000 noise-added $L_{typical}$ spectra were created and processed

to generate $R_{RS}(547)$ using SeaDAS and the MODIS default gain configuration. These same spectra were also processed using the gain suite with $g(869) = 0.946$, with the $R_{RS}(547)$ mean at each SNR and geometry configuration calculated. For SNR-based analyses, we considered specific geometry configurations (θ_S from $0° - 50°$ in $10°$ increments, θ_V from $10° - 70°$ in $10°$ increments, and $\Delta\Phi$ from $0° - 180°$ in $30°$ increments), while geometry-only analyses considered the full possible range of these parameters in $1°$ increments. In these analyses, atmospheric and meteorologic parameters were fixed at global defaults, while windspeed was set at $3 \mathrm{~m~s^{-1}}$.

Finally, to contextualize results, we processed all MODIS and VIIRS data from January and July 2013. As these two sensors have strictly controlled orbits [15], these data show representative winter and summer radiant path geometries (θ_S, θ_V, and $\Delta\Phi$) throughout the entire time series (Fig. 1). Notably, MODIS θ_S is predominantly higher than that of VIIRS at comparable low latitudes (e.g., 20°S in the winter, 20°N in the summer). While both satellites have nominal equatorial overpass at 13:30 local solar time, Aqua's overpass is typically ~9 minutes later than SNPP's [15], resulting in the larger θ_S for MODIS/A. Additionally, $\Delta\Phi$ differences manifest from the larger inclination angle for VIIRS (~98.7°) relative to MODIS (~98.2°) [15]. Data frequency for MODIS is stable among the range of θ_S. VIIRS, however, has higher data frequency for $\theta_S > 32°$ and especially $\theta_S > 45°$ due to the pixel aggregation scheme [12], [16].

III. RESULTS

A. VIIRS g(NIR_L) sensitivity

Gyre-specific VIIRS $\bar{x}$ $R_{RS}(551)$ did not substantially vary among the gain suites tested, with the dominant signal being a steady increase in $\bar{x}$ for all gyres as $g(862)$ increased from $0.975 - 1.0375$ (Fig. 2a). For N Pac, this increase was part of a larger
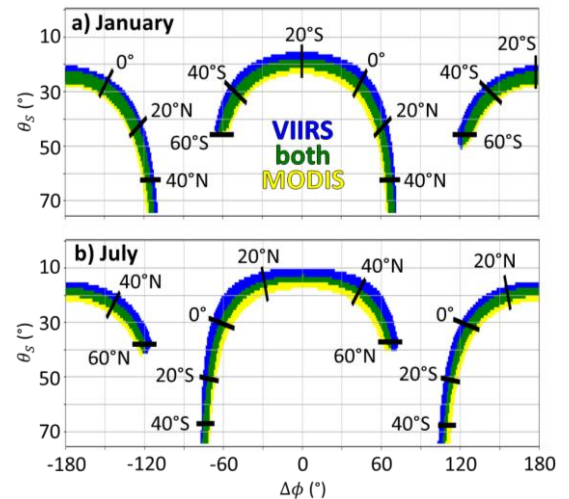

Fig. 1. Radiant path geometries of VIIRS (blue), MODIS (yellow), and their overlap (green) in (a) January and (b) July 2013. Shaded areas contain any geometry accounting for $\geq 0.01\%$ of all pixels with $\theta_V < 40°$ in the month. Tick marks indicate approximate geographic (latitudinal) position where such geometry conditions were experienced. The colored area in the center of these panels (*i.e.*, where $|\Delta\Phi| < 80°$) represent southwest-of-nadir pixels, while the remaining areas represent northeast-of-nadir pixels. Note inverse y-axes.
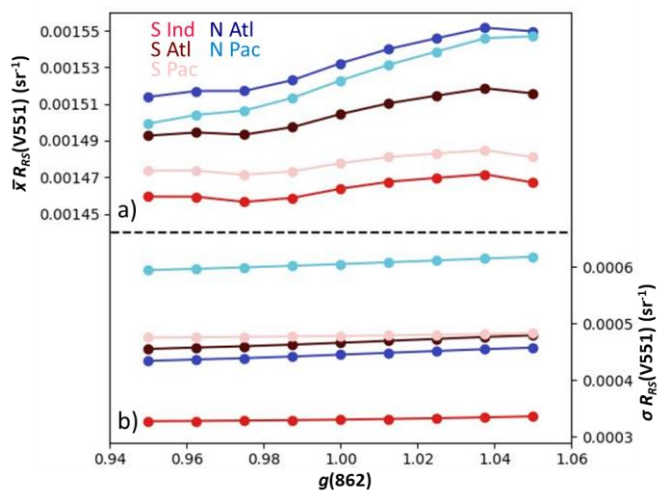
Fig. 2. Sensitivity of VIIRS $R_{RS}(551)$ to changes in $g(NIR_L)$. (a) Gyre-specific mean $R_{RS}(V551)$ generally increase with increasing $g(862)$. (b) $R_{RS}(V551)$ standard deviations show slight increases with increasing $g(862)$. Color indicates gyre.

increasing trend which spanned the full range of $g(862)$ tested. For all gyres, $\sigma R_{RS}(551)$ increased with increasing $g(862)$, albeit very slightly, throughout the span of gain suites tested (Fig. 2b). Both MAPD (Fig. 3) and MAD also showed slight increases with increasing $g(862)$ for all gyres. Accordingly, MAD and MAPD for 'all gyres' (calculated by combining data from all 5 gyres, green line in Fig. 3) showed a similar increasing trend.

B. Cross-sensor comparisons

These results were compared to those reported for MODIS in [8], with particular focus on gain configurations with $g(M869)$ between 0.946 and 1.042, which is roughly comparable to the $g(V862)$ range tested. With the substantial caveat that the VIIRS results are based on substantially more data points than those for MODIS (at least four orders of magnitude, see section IV.C.), we noted some differences between MODIS and VIIRS results in both pattern and magnitude. Specifically, opposite to the trend for VIIRS $\bar{x}$, MODIS $\bar{x}$ decreased with increasing $g(NIR_L)$. Additionally, the percent change in MODIS $\bar{x}$ with increasing $g(869)$ (-2.2 – -3.9%) were generally larger than corresponding VIIRS $R_{RS}(551)$ $\bar{x}$ increases (0.9 – 3.2%; Fig. 2a).
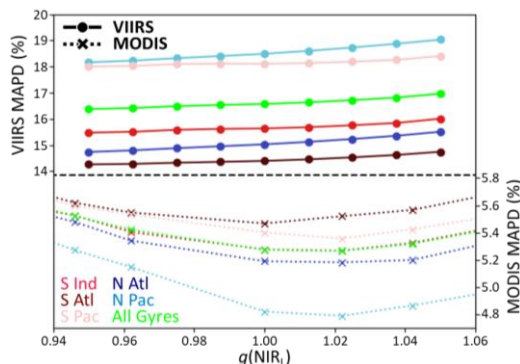

Fig. 3. Gyre-specific mean absolute percent differences (MAPD; %) according to gain suite. VIIRS data show slight increases with increasing $g(862)$. MODIS MAPD (from [8], based on data from 25 discrete locations) are substantially lower than VIIRS MAPD, and generally show minima for gain suites with $g(869) = 1.022 \pm 0.02$.

MODIS σ showed minima in all gyres for $g(869) = 1.00$, while VIIRS σ was minimal at $g(862) = 0.95$, increasing steadily throughout the range of $g(862)$ tested (Fig 2b). Of note, however, VIIRS σ was substantially larger than MODIS σ, with gyre-specific differences ranging from two-fold (S Ind) to five-fold (N Pac). Similarly, MODIS MAD and MAPD for most gyres were minimal for the datasets with $g(869) = 1.022$ (Fig. 3, bottom), while VIIRS MAD and MAPD increased with increasing $g(862)$ (Fig. 3, top). Again, however, the differences in magnitude were substantial, with VIIRS MAPD higher than corresponding MODIS data by at least 2.5 fold. VIIRS autocorrelation coefficient was essentially flat among the different gain suites tested, with magnitudes of ~0.03 (N Pac) to 0.12 (N and S Atl). In contrast, MODIS r showed substantial increases with increasing $g(869)$; gyre-specific r values ranged from ~0.12 – 0.25 for $g(869) = 0.946$, and ~0.2 – 0.35 for $g(869) = 1.046$.

Incorporating SeaWiFS into these comparisons, results were limited to metrics directly calculable from the previous SeaWiFS analysis, namely MCs and hemispheric $\bar{x}$. For this assessment, we considered ± ~5% changes in $g(NIR_L)$, whereby "alternate" MCs were compared to those created with the default gain suites [i.e., $g(NIR_L) = 1.00$]. Notably, the SeaWiFS dataset considered here was not restricted to the specific gyres included in the MODIS and VIIRS analysis, but instead includes a range of geographic subsets [17], identified in Fig. 4 only by hemisphere.

For all sensors and locations, MC ratio patterns were largely mirrored between the -5% (solid lines in Fig. 4) and +5%
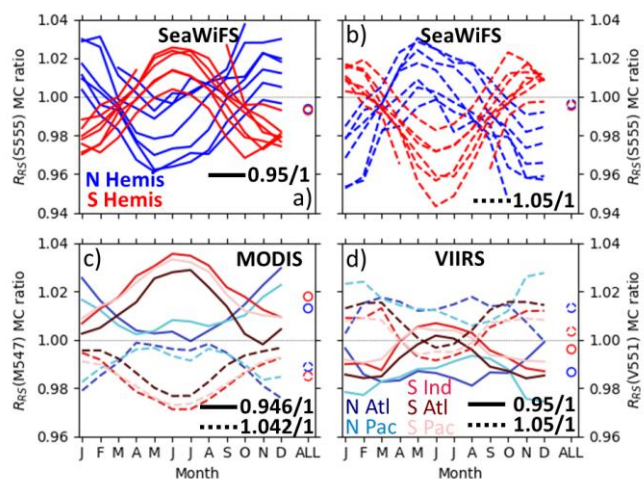

Fig. 4. Sensitivity of R_{RS}(green) to ~5% changes in $g(NIR_L)$. These panels show ratios in R_{RS} monthly climatologies (MC), calculated using datasets with $g(NIR_L) \approx 0.95$ / the same pixels processed with $g(NIR_L) = 1.00$ (solid lines) and $g(NIR_L) \approx 1.05$ / $g(NIR_L) = 1.00$ (dotted lines) for (a-b) SeaWiFS, (c) MODIS, and (d) VIIRS. Ratios based on the entire dataset, separated by hemisphere, shown as circles labeled 'ALL.' Blue shades indicate Northern Hemisphere regions, while reds are Southern Hemisphere (for MODIS and VIIRS, the gyre-specific color scheme is retained from Figs 1-2). In general, the 0.95/1.00 ratio is low in the respective (austral or boreal) summer as compared to winter, while the 1.05/1.00 ratio shows the opposite seasonal pattern. SeaWiFS ratios have larger magnitude than either MODIS or VIIRS (note different y-axis scales for (a-b) as compared to (c-d)). Seasonal effects are similar in magnitude for MODIS and VIIRS, but VIIRS ratios, especially in the Southern Hemisphere, are more centered around a ratio of 1 (as are SeaWiFS).

(dotted lines in Fig. 4) $g(NIR_L)$ configurations, with comparable magnitude but opposite direction of impact. Similarly, results between NH and SH gyres were generally mirrored, with $g(NIR_L) = 0.95$ / $g(NIR_L) = 1.00$ MC ratios low in the summer (austral or boreal) as compared to winter. This seasonal pattern was reversed when comparing default MC to those created from the $g(NIR_L) = 1.05$ dataset. The sole exceptions to this pattern were the VIIRS N Hemisphere gyres: N Pacific MC ratios showed the opposite seasonal trend to that observed for other regions and sensors, while N Atlantic ratios were flat throughout most of the year. The range of MC ratios was considerably larger for SeaWiFS (-0.94 – 1.04; Fig. 4a-b) and MODIS (-0.95 – 1.04; Fig 4c) relative to VIIRS (-0.98 – 1.02; Fig. 4d). Additionally, the SeaWiFS and VIIRS ratios were generally centered around 1.0 (with the exception of VIIRS NH), while the alternate MODIS datasets were uni-directionally biased, relative to the default, throughout the year (circles in Fig. 4).

C. Geometry and SNR

From the cross-sensor comparisons, we observed varying degrees of $g(NIR_L)$ sensitivity for all three satellite sensors. As part of objective 3, we performed simulations to determine if any of the cross-sensor similarities and differences in $g(NIR_L)$ sensitivity were attributable to instrument-independent factors. We thereby assessed radiant path and SNR impacts on $g(NIR_L)$ sensitivity directly, processing $L_{typical}$ [14] to derive $R_{RS}(547)$ at various SNRs, θ_S, θ_V, and $\Delta\Phi$.

From these analyses, we observed varying sensitivity to $g(NIR_L)$ resulting from each parameter tested (Fig. 5). Note that in this visualization, higher $g(NIR_L)$ sensitivity is observed for any deviation (positive or negative) from a mean ratio of 1.0. For example, little sensitivity was noted for $\theta_V \geq 30°$, as the mean ratio was approximately 1.0 [i.e., $R_{RS}(547)$ was the same regardless of the gain suite] (Fig. 5b). Sensitivity increased (as mean ratio increased) at larger θ_V. For $\Delta\Phi$, the largest sensitivity
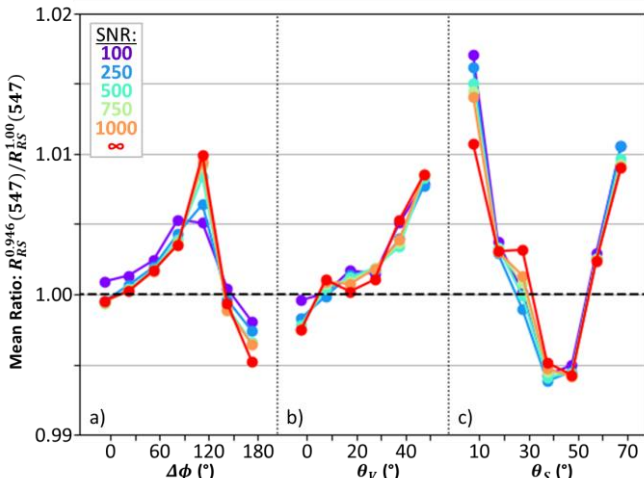
was observed at 120°, with the mean ratio being relatively high (> 1.005). A prominent seasonal signal was also identified, manifesting as θ_S sensitivity, whereby the mean ratio was notably high (> 1.01) for $\theta_S = 10°$ and 70°, and low (<0.995) for θ_S of 30° and 40°. SNR sensitivity was restricted to specific geometries, particularly $\Delta\Phi = 120°$, $\theta_S = 10°$, and $\theta_S = 30°$, with mean ratios generally increasing with increasing SNR.

This visualization (Fig 5) shows impacts of both SNR and radiant path geometry, as well as their interaction, on the sensitivity of an $R_{RS}(547)$ dataset to changes in $g(NIR_L)$. However, due to orbital characteristics, not all radiant path geometries are equally likely (or even possible) for a given sensor. Indeed, as MODIS and VIIRS orbits are regularly modified to correct drift [15], only a very narrow range of geometries are observed (Fig. 1). While these prevailing geometries are quite similar between the two sensors (green overlap in Fig. 1), there are substantial differences, detailed in section II.C.

Filling the geometric intervals from the previous visualization (Fig. 5), Fig. 6 indicates $g(NIR_L)$ sensitivity for the full suite of possible $\Delta\Phi$ and θ_S, overlain by the prevailing satellite geometries. Unsurprisingly, the trends observed in Fig. 6 are consistent with those in Fig. 5, while providing some context to the noted impacts of radiant path geometry on $g(NIR_L)$ sensitivity. For example, the $R_{RS}(547)$ ratio [$R_{RS}(547)$ derived from $L_{typical}$ with $g(NIR_L) = 0.95$ / that with $g(NIR_L) = 1.00$] was generally low (~0.99) for geometries with θ_S with between 40° and 50° (horizontal blue regions in all three panels of Fig. 6) and high (>1.01) for θ_S greater than 60° or less than 15°. The $R_{RS}(547)$ ratio was also generally more stable at low θ_V, and where $|\Delta\Phi| < 120°$.

IV. DISCUSSION

A. VIIRS g(NIR_L) sensitivity

Overall, these results indicate moderate sensitivity of VIIRS $R_{RS}(551)$ to changes in $g(862)$, particularly in the Northern Hemisphere. This sensitivity manifests as generally increasing $\bar{x}$ with increasing $g(862)$. The lack of variability in σ
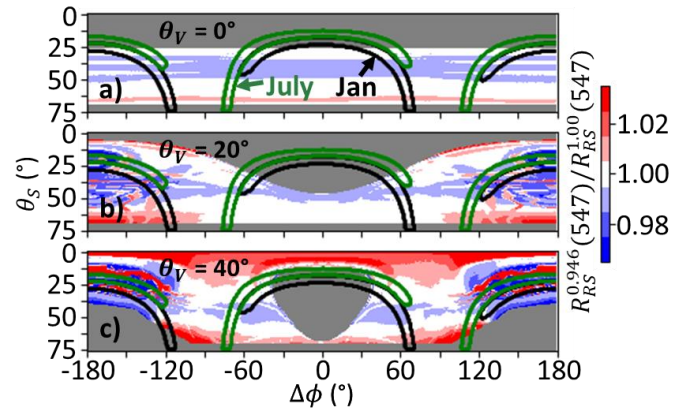

Fig. 5. Effect of radiant path geometry and NIR SNR on $g(NIR_L)$ sensitivity. Each symbol corresponds to a ratio of mean $R_{RS}(547)$ values derived from simulations using two separate gain suites at specific SNR (color) and radiant path configurations ($N = 294$). The same data points are displayed in all three panels, separately binned according to (a) $\Delta\Phi$, (b) θ_V, and (c) θ_S. Spectra were excluded if processing $L_{typical}$ resulted in L3-flagged R_{RS} (windspeed = 3 m s^{-1}).

Fig. 6. Effect of radiant path geometry on $g(NIR_L)$ sensitivity. Underlying maps show the ratio of $R_{RS}(547)$ (as processed from $L_{typical}$ using two different gain suites) for all possible combinations of $\Delta\Phi$ and θ_S, and at θ_V = (a) 0°, (b) 20°, and (c) 40°. Grey indicates L3-flagged R_{RS} (windspeed = 3 m s^{-1}). Overlain contours show distribution of MODIS geometries in January (black) and July (green). Contours contain any geometry accounting for ≥ 0.01% of all pixels with $\theta_V < 40°$ in the month.

concomitant with these $\bar{x}$ changes is consistent with simple $R_{RS}(551)$ offsets resulting from gain configuration alterations. At the individual pixel / spectrum level, however, increasing $g(862)$ (followed by subsequent SVC) could have either positive or negative impacts on the retrieved $R_{RS}(551)$. In the aggregate, gyre-specific $\bar{x}$ changes, over the range of $g(862)$ tested, were all < 3.2% (Fig. 2a). Gyre-specific monthly climatology changes were also relatively small: generally < 2% for a 5% $g(862)$ change in either direction (Fig 4d). These values are within the 5% target uncertainty for satellite-derived R_{RS} in the visible wavebands [18]. Nevertheless, these results indicate that g(NIR$_L$)-based impacts can comprise a substantial portion of the uncertainty budget.

B. Identifying an optimal VIIRS g(NIR$_L$)

Using r and MAD (or MAPD, which reduces the impact of differences in magnitude) to operationalize temporal stability of time series in ocean gyres, we note that none of the $R_{RS}(551)$ time series considered here was substantially more 'realistic' than the others. We observed no inflection points or minima in these parameters that might suggest a benefit to changing $g(862)$, which is contrary to the MODIS findings of an optimal $g(869) = 1.025 \pm 0.02$.

Three obvious reasons for this null finding for VIIRS include: (1) an optimal $g(862)$ exists, but is outside the range of values tested (likely < 0.95); (2) the higher variability in the VIIRS R_{RS} data themselves, relative to MODIS, obscures any impact of changing $g(NIR_L)$; or (3) structural differences in satellite orbit and / or instrument design are impacting results. For the first, note (Table I) that none of the current default VIIRS SVC gains is < 0.95 or > 1.05, with the mean gain being 0.981 ($\sigma = 0.013$). Assuming $g(862) = 0.95$, the flat shapes of the MAPD (Fig. 3) and r curves indicate that the uncertainty around that determination would be quite large (at least ± 0.05), and would include the current $g(V862) = 1.00$. It is nevertheless possible that a $g(862) < 0.95$ exists, potentially with a lower uncertainty, but this would only be indicated by MAPD and r changes of magnitude not observed within the $g(862)$ range tested. Relatedly, note that several cross-calibration studies [9]–[11] have found that VIIRS total radiance (L_t) data at 862 nm are approximately 3-3.5% higher than band-shifted MODIS $L_t(869)$. Setting $g(V862) \leq 0.95$ would thus require setting $g(M869) \leq 0.985$, a value which would be detrimental to the temporal stability of the MODIS $R_{RS}(547)$ dataset [8], and likely have little impact on the VIIRS $R_{RS}(551)$ dataset other than a slight decrease in magnitude.

More likely is the second possibility, that VIIRS $R_{RS}(551)$ are substantially more variable than MODIS $R_{RS}(547)$, which obscures any potential signal in r, MAD, or MAPD according to $g(862)$. This is evidenced by the much larger magnitude of VIIRS σ compared to MODIS σ (ranging from 2-fold to 5-fold). Indeed, regardless of gain suite, day-to-day $R_{RS}(V551)$ means, synoptically covering entire ocean gyres, are less autocorrelated (lower r) than a sparse time series of $R_{RS}(M547)$ measurements within those same gyres. Similarly, these daily mean $R_{RS}(V551)$ have much larger deviation from their 31-day moving mean (higher MAD, MAPD) than corresponding MODIS data, again, as based on a substantially smaller dataset. These differences

are likely attributable to differences in green band SNR between the two sensors (MODIS SNR for the 547 band is 2402 [14], while SNR for the VIIRS 551 band is ~1020, calculated using the same approach as [14]). Note that any green band SNR differences would most likely impact the magnitude of R_{RS}(green) summary statistics (e.g., Figs. 2 – 3) irrespective of $g(NIR_L)$. Owing to the role of $L_t(NIR_L)$ in atmospheric correction, differences in NIR$_L$ SNR (806 and ~450 for MODIS and VIIRS, respectively [14]) may result in $g(NIR_L)$-dependent impacts on R_{RS}(green) time series,. As such, our SNR-based simulations were intended to assess the relationship between such R_{RS}(green) variability and $g(NIR_L)$ sensitivity (Fig. 5). Similarly, the potential impact of differences in satellite orbit (reason 3, above) on $g(NIR_L)$ sensitivity were investigated via the geometry-based simulations (Figs. 5-6).

C. Comparability of analyses

Despite sharing a general framework (*i.e.,* the 4 steps listed in Section II), the individual sensor analyses were each conducted using a unique methodology. As a result, we structured our analyses to minimize potential methodological impacts on our interpretation of cross-sensor similarities and differences in $g(NIR_L)$ sensitivity. In particular, where possible, we used only metrics and $g(NIR_L)$ ranges which were shared among the various analyses. For example, when comparing SeaWiFS data to MODIS and VIIRS, we only considered two metrics (MCs and hemispheric $\bar{x}$) and three $g(NIR_L)$ values (~0.95, 1.00, and ~1.05). Additionally, the MODIS dataset as developed in [8] included many interpolated band suites, but only those directly calculated via SVC were used here. Standardization of other methodological factors, however, was not as straightforward. In particular, the processing version (R2010.0 for SeaWiFS, R2018.0 for MODIS and VIIRS), data exclusion regime (L3 mask for SeaWiFS and VIIRS, L2 Flags = 0 for MODIS), and spatial resolution / geographical range (global 4 km resolution for SeaWiFS; 1 km resolution at 25 gyre locations for MODIS; 750 m resolution within gyres for VIIRS) all differed among the various assessments.

Primarily as a result of the geographic range and resolution differences, the VIIRS parameters derived in this study represented four orders of magnitude more data than those from the MODIS analysis [8]. SeaWiFS data quantity was somewhere between these two. To ensure fair comparison between MODIS and VIIRS, we subset our VIIRS dataset to mimic the station count and data exclusion criteria from [8]. In doing so, we noted some resultant variation in summary statistics between the full VIIRS dataset and the subset, but no substantial differences in either magnitude of parameters or trends relative to $g(862)$, giving credence to the MODIS / VIIRS comparisons detailed above. This also indicates sensitivity to $g(NIR_L)$ changes in ocean gyres can be detected without full mission reprocessing.

D. Cross-sensor sensitivity differences

Taken together, the combined analyses of SeaWiFS, MODIS, and VIIRS highlight that all sensors show some $g(NIR_L)$ sensitivity, but that scale is important when

considering cross-sensor differences. For example, as reported in [8], we observed that R_{RS}(green) may vary by ± 10% when derived for single pixel processed with gain suites having ± 5%. Aggregating data to consider full timeseries (i.e., using $\bar{x}$), however, this sensitivity is much more moderate. In this context, the most substantial g(NIR$_L$) sensitivity was observed for VIIRS NH gyres and all MODIS gyres. In contrast, VIIRS SH gyres and global SeaWiFS data show little change in $\bar{x}$ with changes in g(NIR$_L$). However, at the level of monthly climatologies, all sensors show substantial g(NIR$_L$) sensitivity, with SeaWiFS being the most prominently impacted (Fig. 4).

In addition to scale, the manner in which g(NIR$_L$) impacts downstream geophysical parameters is not consistent in magnitude or direction. As a primary example, $\bar{x}$ R_{RS}(V551) slightly increased with increasing g(NIR$_L$) (Fig. 2a), while $\bar{x}$ R_{RS}(M547) steadily decreased with similar g(NIR$_L$) increases. This particular finding highlights the complexities of ensuring cross-sensor continuity of R_{RS}(green) by modifying g(NIR$_L$). While knowing and correcting for an NIR$_L$ offset between sensors can improve R_{RS}(green) continuity [11], that same offset, corrected using different absolute calibrations, may have slightly different impacts on the final R_{RS}(green) continuity.

For all sensors and at the largest scale, our results are broadly consistent with the conclusions of [6] that R_{RS}(visible) are acceptably resilient to 5% changes in g(NIR$_L$). Specifically, on the scale of individual gyres (Fig 2a) or hemispheres (circles in Fig. 4), setting g(NIR$_L$) ± 5% resulted in $\bar{x}$ R_{RS}(green) changes which were within target mission uncertainties of 5% in R_{RS}(visible) [18]. Again, however, these moderate impacts on aggregated data (e.g., $\bar{x}$) belie much larger sensitivities at the scale of individual spectra or monthly climatologies (lines in Fig. 4). For SeaWiFS, MODIS, and VIIRS, a single 5% change (+ or -) in g(NIR$_L$) can result in R_{RS}(green) MCs varying, over the course of a year, by 7-10%, 3-4%, or ~2%, respectively (Fig. 4). For individual months, changing from +5% to -5% g(NIR$_L$) results in gyre-specific MC changes on the order of ± 9%, 0-6 %, and ± 5% for SeaWiFS, MODIS, and VIIRS, respectively (Fig 4).

Overall, the most prominent signals conserved across all satellite-based analyses were the seasonally harmonic patterns (Fig. 4). Namely, with few exceptions, decreasing g(NIR$_L$) by ~5% caused wintertime increases in R_{RS}(green). This is in contrast to summertime, where such a g(NIR$_L$) resulted R_{RS}(green) which was either lower (SeaWiFS and VIIRS S Hemisphere) or unchanged (MODIS) from the default dataset. This seasonal pattern strongly indicates radiant path geometry (which would vary according to season and hemisphere) as one causal factor in g(NIR$_L$) sensitivity.

E. Potential underlying causes for g(NIR$_L$) sensitivity

As noted, g(NIR$_L$) sensitivity appeared to include a geometry component, evidenced by prominent seasonal and hemispheric effects (Fig. 4). Cross-sensor g(NIR$_L$) sensitivity differences may thus be traceable to different prevailing radiant path geometries for individual satellites (Fig. 1). Additionally, the three sensors studied also have substantially different SNRs, which might also contribute to cross-sensor differences in

g(NIR$_L$) sensitivity. Due to the noted scale-dependent difficulties in assessing g(NIR$_L$) sensitivity using real satellite data, the simulation analyses performed in this study directly quantify impacts of these potential underlying causes for g(NIR$_L$) sensitivity.

From these simulation studies, we observed impacts of SNR (Fig. 5) and radiant path geometry (Figs. 5 & 6) on g(NIR$_L$) sensitivity. The SNR impacts also included a geometry component, as they were only noted for certain discrete geometries ($\Delta\Phi = 120°$, $\theta_S = 10°$, and $\theta_S = 30°$). Recalling that $\theta_S = 10°$ is uncommon in real satellite data (Fig. 1), higher SNRs generally resulted in higher g(NIR$_L$) sensitivity. This is broadly consistent with our findings that MODIS data (at the $\bar{x}$ scale) are more sensitive to g(NIR$_L$) changes than VIIRS or SeaWiFS.

The heterogeneity observed in the geometry-only simulations (Fig. 6) highlights that the discrete geometries tested in the SNR analysis (Fig. 5) are not fully representative of trends in geometric g(NIR$_L$) sensitivity. More importantly, MODIS and VIIRS geometries frequently overlay regions of extreme and variable g(NIR$_L$) sensitivity, particularly for the northeastern portion of their swaths ($|\Delta\Phi| > 120°$) at $\theta_V \geq 20°$ (Fig. 6b,c). Thus, even though the prevailing geometries of MODIS and VIIRS have substantial overlap (Fig. 1) the impact of even slight differences in geometry may be appreciably impacting overall g(NIR$_L$) sensitivity. Additionally of note, the SNR and geometry impacts reported here correspond to a single $L_{typical}$, and are likely not fully consistent for all radiance spectra.

F. Recommendations

While the three analyses using actual satellite data indicate varying levels of g(NIR$_L$) sensitivity, the simulations highlight that extraneous factors (particularly radiant path geometry) can contribute to any noted sensitivity. These geometric impacts are understandable in the context of satellite data processing, whereby radiant path geometry is an explicit factor in derivation of several coefficients and intermediate products. Additionally, L_t(NIR$_L$) [which is directly modulated by g(NIR$_L$)] is a precursor to aerosol model selection and calculation of aerosol radiance (L_a) contributions across the visible wavebands. Ideally, SVC of the visible bands should nullify these g(NIR$_L$) impacts, at least in the context of 5% mission target uncertainties in R_{RS}(visible) [6], [18]. Recalling that the purpose of SVC is to remediate a systematic bias in the coupled instrument-atmospheric correction system, the geometry-dependent uncertainties noted here (Figs 5 & 6) manifest from atmospheric correction impacts and cannot be resolved through SVC.

Nevertheless, our studies indicate relevant uncertainties (particularly on the scale of monthly climatologies) related to g(NIR$_L$) changes of ± 5%. These impacts may contribute to residual seasonality (relative to the MOBY timeseries) noted in the SeaWiFS, MODIS, and VIIRS R_{RS} datasets [19]. In practice, g(NIR$_L$) sensitivity should be considered in R_{RS} uncertainty budgets for all sensors, but is likely to have more substantial impacts for instruments with higher NIR SNR and / or prevailing radiant path geometries for which higher sensitivity is predicted. Sensitivity analyses need not include full mission

reprocessing, but must ensure that the pixels assessed have radiant path geometries representative of the larger dataset.

While $g(\text{NIR}_L)$ sensitivity studies (as performed in the current work) can reliably identify impacts of modifying $g(\text{NIR}_L)$ on R_{RS} timeseries (Figs 2 - 4), they are not always suited for calculating a calibration coefficient for the NIR_L band. While the MODIS-based analysis identified an optical $g(\text{M869})$ with determined accuracy of $\pm\ 0.02$, accuracy for a similarly defined $g(\text{V862})$ would be greater than $\pm\ 0.05$. This is larger than that which could be by achieved using a sun photometer to calibrate the NIR_L band ($> \pm\ 0.02$; [20]–[22]). This means that rigorous, universally applicable methods to identify $g(\text{NIR}_L)$ remain elusive. Therefore, once $g(\text{NIR}_L)$ for a specific sensor has been confidently established, simultaneous same view (SSV) analyses [11] should be employed to provide precise calibration coefficients for additional sensors. Nevertheless, even after cross-calibration of NIR_L bands, additional effort is essential to remediate remaining biases between satellite R_{RS} datasets [11]. Future satellite missions should also consider the impact of NIR SNR on retrievals, including impacts of similar SVC assumptions in multi-band atmospheric correction algorithms [23].

V. CONCLUSIONS

This study directly assesses a fundamental assumption (insensitivity of R_{RS}(green) to moderate $g(\text{NIR}_L)$ changes) employed in vicarious calibration and atmospheric correction of satellite ocean color data. We highlight that the impact of this assumption on satellite ocean color datasets depends on individual sensor / orbit characteristics and the aggregation scale being considered (individual spectra to global composites). The findings emphasize the importance of establishing an accurate $g(\text{NIR}_L)$ for some (but not all) sensors, as well as the difficulty in doing so. As such, we recommend a multi-faceted approach to minimizing the impact of $g(\text{NIR}_L)$ sensitivities on satellite ocean color datasets.

VI. ACKNOWLEDGMENT

VII. REFERENCES

[1] W. W. Gregg and N. W. Casey, "Improving the consistency of ocean color data: A step toward climate data records," *Geophys. Res. Lett.*, 2010.

[2] S. R. Signorini, B. A. Franz, and C. R. McClain, "Chlorophyll variability in the oligotrophic gyres: mechanisms, seasonality and trends," *Front. Mar. Sci.*, vol. 2, no. February, pp. 1–11, 2015.

[3] B. B. Barnes and C. Hu, "Cross-sensor continuity of satellite-derived water clarity in the Gulf of Mexico: Insights into temporal aliasing and implications for long-term water clarity assessment," *IEEE Trans. Geosci. Remote Sens.*, vol. 53, no. 4, pp. 1761–1772, 2015.

[4] B. B. Barnes and C. Hu, "Dependence of satellite ocean color data products on viewing angles: A comparison between SeaWiFS, MODIS, and VIIRS," *Remote Sens. Environ.*, vol. 175, 2016.

[5] F. Mélin, G. Sclep, T. Jackson, and S. Sathyendranath, "Uncertainty estimates of remote sensing reflectance derived from comparison of ocean color satellite data sets," *Remote Sens. Environ.*, 2016.

[6] M. Wang and H. R. Gordon, "Calibration of ocean color scanners: How much error is acceptable in the near infrared?," *Remote Sens. Environ.*, vol. 82, no. 2–3, pp. 497–504, 2002.

[7] B. A. Franz, S. W. Bailey, P. J. Werdell, and C. R. McClain, "Sensor-independent approach to the vicarious calibration of satellite ocean color radiometry.," *Appl. Opt.*, vol. 46, no. 22, pp. 5068–82, Aug. 2007.

[8] B. B. Barnes, C. Hu, S. W. Bailey, and B. A. Franz, "Sensitivity of Satellite Ocean Color Data to System Vicarious Calibration of the Long Near Infrared Band," *IEEE Trans. Geosci. Remote Sens.*, 2020.

[9] N. Pahlevan *et al.*, "Landsat 8 remote sensing reflectance (Rrs) products: Evaluations, intercomparisons, and enhancements," *Remote Sens. Environ.*, 2017.

[10] A. M. Sayer *et al.*, "Cross-calibration of S-NPP VIIRS moderate-resolution reflective solar bands against MODIS Aqua over dark water scenes," *Atmos. Meas. Tech.*, 2017.

[11] B. B. Barnes, C. Hu, S. W. Bailey, N. Pahlevan, and B. A. Franz, "Cross-calibration of MODIS and VIIRS long near infrared bands," *Remote Sens. Environ.*, 2021.

[12] B. B. Barnes, J. P. Cannizzaro, D. C. English, and C. Hu, "Validation of VIIRS and MODIS reflectance data in coastal and oceanic waters: An assessment of methods," *Remote Sens. Environ.*, vol. 220, no. October 2018, pp. 110–123, 2019.

[13] NASA and OBPG, "convert_band.c." [Online]. Available: https://oceancolor.gsfc.nasa.gov/docs/ocssw/convert__band_8c_source.html. [Accessed: 11-Nov-2020].

[14] C. Hu *et al.*, "Dynamic range and sensitivity requirements of satellite ocean color sensors: learning from the past.," *Appl. Opt.*, vol. 51, no. 25, pp. 6045–62, Sep. 2012.

[15] X. Shao, C. Cao, X. Xiong, B. Zhang, S. Uprety, and T.-C. Liu, "Orbital variations and impacts on observations from SNPP, NOAA 18-20, and AQUA sun-synchronous satellites," *Proc. SPIE 10764*, no. September, pp. 1–9, 2018.

[16] C. Cao *et al.*, "Visible Infrared Imaging Radiometer Suite (VIIRS) Sensor Data Record (SDR) User's Guide, Version 1.2. NOAA Technical Report NESDIS 142," Washington, D.C., 2013.

[17] B. A. Franz, "Methods for Assessing the Quality and Consistency of Ocean Color Products," 2009. [Online]. Available: https://oceancolor.gsfc.nasa.gov/docs/methods/sensor_analysis_methods/. [Accessed: 06-Mar-2021].

[18] S. B. Hooker and W. E. Esaias, "An overview of the SeaWiFS Project," *Eos, Transactions American Geophysical Union*, vol. 74, no. 21. p. 241, 1993.

[19] K. M. Bisson, E. Boss, P. J. Werdell, A. Ibrahim, R. Frouin, and M. J. Behrenfeld, "Seasonal bias in global ocean color observations," *Appl. Opt.*, vol. 60, no. 23, p. 6978, 2021.

[20] H. R. Gordon and T. Zhang, "How well can radiance reflected from the ocean–atmosphere system be predicted from measurements at the sea surface?," *Appl. Opt.*, vol. 35, no. 33, p. 6527, 1996.

[21] N. Martiny, R. Frouin, and R. Santer, "Radiometric calibration of SeaWiFS in the near infrared," *Appl. Opt.*, vol. 44, no. 36, p. 7828, 2006.

[22] R. Santer and N. Martiny, "Sky-radiance measurements for ocean-color calibration – validation," *Appl. Opt.*, vol. 42, no. 6, pp. 896–907, 2003.

[23] A. Ibrahim, B. A. Franz, Z. Ahmad, and S. W. Bailey, "Multiband atmospheric correction algorithm for ocean color retrievals," *Front. Earth Sci.*, 2019.

Brian B. Barnes received the B.S. degree in zoology and psychology from the University of Florida, Gainesville, FL, USA, in 2004, the M.S. degree in marine science from the College of William and Mary, Virginia Institute of Marine Science, Gloucester Point, VA, USA, in 2009, and the Ph.D. degree in marine science from the University of South Florida, St. Petersburg, FL, USA, in 2013.

He is currently a Research Associate with the Optical Oceanography Laboratory, College of Marine Science, University of South Florida. His research interests include calibration and validation of ocean color satellite data toward enhanced coastal research and monitoring.

Sean W. Bailey received a Bachelor of Science degree in marine science and biology from the University of Miami in 1992 and a Master of Science degree (biological oceanography) from the University of Southern Mississippi in 1997.

He joined NASA's Goddard Space Flight Center in 1997 as a contractor working for what is now the Ocean Biology Processing Group. His research interests are focused on bio-optical remote sensing of the oceans, specifically with the on-orbit calibration of satellite-based sensors and the validation of their data products. In 2015, he became a civil servant with NASA and currently serves as the manager for the Ocean Biology Distributed Active Archive Center.

Chuanmin Hu received a BS degree in physics from the University of Science and Technology of China in 1989 and a PhD degree in physics (environmental optics) from the University of Miami (Florida, USA) in 1997. He is currently a professor of optical oceanography at the University of South Florida (USA), who also directs the Optical Oceanography Lab. He uses laboratory, field, and remote sensing techniques to study marine algal blooms (harmful and non-harmful, macroalgae and microalgae), oil spills, coastal and inland water quality, and global changes. Between 2009 and 2014 he served as a topical editor on ocean optics and ocean color remote sensing at *Applied Optics*, and between 2015 and 2017 he served as a chief editor at *Remote Sensing of Environment*.

Bryan A. Franz is a Research Scientist and Assistant Chief for Science Research in the Ocean Ecology Laboratory at NASA Goddard Space Flight Center. Since 1996, he has supported research and operations for satellite remote sensing of ocean biology and biogeochmistry at NASA, including the development of science data products from the Sea-viewing Wide Field-of-view Sensor (SeaWiFS), Moderate Resolution Imaging Spectroradiometer (MODIS), Medium Resolution Imaging Spectrometer (MERIS), Visible and Infrared Imaging Radiometer Suite (VIIRS), and other satellite-based remote sensing radiometers. Since 2009 he has served as the Ocean Discipline Leader for the MODIS Science Team and the combined MODIS and VIIRS Science Team, and he is currently leading the development of the Science Data Segment (SDS) for the Plankton, Aerosol, Cloud, ocean Ecosystem (PACE) mission.

His work at NASA has focused on standardization of atmospheric correction and bio-optical algorithms, vicarious calibration, and instrument cross-calibration techniques to derive consistent, multi-mission time-series of ocean optical and biogeochemical properties.